A new B-dot probe-based diagnostic for amplitude, polarization, and wavenumber measurements of ICRF fields on ASDEX Upgrade

R. Ochoukov[1], V. Bobkov[1], H. Faugel[1], H. Fünfgelder[1], J.-M. Noterdaeme[1,2], and the ASDEX Upgrade Team[*]

[1]Max-Planck-Institut für Plasmaphysik, Boltzmannstr. 2, 85748 Garching, Germany

[2]UGent, Applied Physics Department, 9000 Gent, Belgium

Abstract:

A new B-dot probe-based diagnostic has been installed on ASDEX Upgrade tokamak to characterize ion cyclotron range-of frequencies (ICRF) wave generation and interaction with magnetized plasma. The diagnostic consists of a field-aligned array of B-dot probes, oriented to measure fast and slow ICRF wave fields and their field-aligned wavenumber ($k_{//}$) spectrum on the low field side of ASDEX Upgrade. A thorough description of the diagnostic and the supporting electronics is provided. In order to compare the measured dominant wavenumber of the local ICRF fields with the expected spectrum of the launched ICRF waves, in-air near-field measurements were performed on the newly installed 3-strap ICRF antenna to reconstruct the dominant launched toroidal wavenumbers (k_{tor}). Measurements during a strap current phasing scan in tokamak discharges reveal an upshift in $k_{//}$ as strap phasing is moved away from the dipole configuration. This result is the opposite of the k_{tor} trend expected from in-air near-field measurements; however, the near-field based reconstruction routine does not account for the effect of induced radiofrequency (RF) currents in the passive antenna structures. The measured exponential increase in the local ICRF wave field amplitude is in agreement with the upshifted $k_{//}$, as strap phasing moves away from the dipole configuration. An examination of discharges heated with two ICRF antennas simultaneously reveals the existence of beat waves at 1 kHz, as expected from the difference of the two antennas' operating frequencies. Beats are observed on both the fast and the slow wave probes suggesting that the two waves are coupled outside the active antennas. Although the new diagnostic shows consistent trends between the amplitude and the phase measurements in response to changes applied by the ICRF antennas, the disagreement with the in-air near-field measurements remains. An electromagnetic model is currently under development to address this issue.

Introduction:

Ion cyclotron range-of frequencies (ICRF) heating is a promising technique to heat magnetically confined plasmas to fusion relevant temperatures. Some of the key advantages of ICRF heating are 1) inexpensive, readily available technology for radiofrequency (RF) wave generation in the 10-100 MHz frequency range; 2) the ability to deposit power to the ions, rather than the electrons in the plasma; and 3) the ICRF wave accessibility to the core region of high density plasmas. The main disadvantage of ICRF heating is the necessity to position the launcher/antenna close to the confined plasma due to the fact that the ICRF wave responsible for core heating is evanescent in the low plasma density region. The combination of finite plasma density near the confined region and strong RF fields near the launcher generate a range of unwanted interactions in tokamaks,

*For authors list, see U. Stroth et al., Nucl. Fusion 53, 104003A (2013).

such as hot spot formations observed on Tore Supra [ref 1], enhanced sputtering observed on Alcator C-Mod [ref 2] and ASDEX Upgrade [ref 3], and local plasma density modifications observed on JET [ref 4]. In all cases non-linear interactions between ICRF wave electric fields and the plasma sheath are suspected to be the cause [ref 5]. While the local plasma parameters (electron temperature, plasma density, and plasma potential) are usually thoroughly diagnosed in the tokamak boundary with either Langmuir probes or spectroscopically, direct measurements of the local ICRF wave field properties (amplitude, polarization, and wavenumber spectra) are often lacking. An appropriate diagnostic choice to measure periodically changing RF magnetic fields directly is a B-dot probe (occasionally called a magnetic loop or a current probe).

ICRF fields have been studied previously in tokamaks using B-dot probe arrays. Examples include: 1) a toroidally aligned array of B-dot probes installed on the high-field side of Alcator C-Mod for studies of ICRF wave absorption and transmission in the plasma core [ref 6]; 2) a passively operated 2-strap antenna on the low-field side of JT-60U for studies of ion cyclotron emission by majority and fusion product ions [ref 7]; and 3) a pair of orthogonally-aligned B-dot and electric dipole probes installed on the low-field side of TEXTOR and ASDEX for studies of parametric decay instabilities [ref 8]. In most cases, the diagnostic focuses on measuring only the fast wave fields, rather than the complete wave field structure. In order to have a better resolved picture of the ICRF wave field structure in the tokamak boundary plasma, it is necessary to have a diagnostic capable of measuring all the relevant local ICRF properties (amplitude, polarization, and wavenumber spectrum) simultaneously.

The goal of the paper is to introduce a newly installed B-dot probe array on ASDEX Upgrade. The purpose of the diagnostic is to measure directly the main properties of the local ICRF wave field: its amplitude, polarization, and wavenumber. Key components and operating principles of the diagnostic are described in detail. The local properties of the measured ICRF wave fields are then compared with the expected properties of the launched ICRF waves. Finally, future prospects for the diagnostic are outlined.

Diagnostic Description:

In order to quantify the properties (amplitude, polarization, and wavenumber spectrum) of ICRF fields in the vicinity of the newly installed 3-strap ICRF antennas on ASDEX Upgrade [ref 9], an array of high frequency B-dot (HFB) probes was mounted toroidally near the antenna. The HFB probe array was installed on the low-field side in Sector 11, approximately midway toroidally between the new 3-strap antenna in Sector 12 and the old 2-strap antenna in Sector 10 (Fig. 1). The probe array is positioned 6 ± 3 cm below the midplane ($Z = 0$ m, Fig. 1) at the major radius $R = 2.286 \pm 0.005$ m, which is 10 cm radially behind the ICRF protection limiter. The probes on the array are positioned to align to the contour of the local magnetic field line (B-field) in a standard ASDEX Upgrade discharge (on-axis toroidal magnetic field $B_T = -2.5$ T, total plasma current $I_P = 1.0$ MA), the resulting array inclination to the horizontal is ~11^o. The array consists of 6 probe pairs and each pair consists of a “fast” and a “slow” wave probe, where the “fast” probe is oriented to be sensitive to the RF magnetic fields aligned parallel to B-field and the “slow” probe is oriented to pick up the RF magnetic fields perpendicular to B-field. The “fast” probes are labeled ‘1’, ‘3’, ‘5’, ‘7’, ‘9’, and ‘11’ and the “slow” probes are ‘2’, ‘4’, ‘6’, ‘8’, and

*For authors list, see U. Stroth et al., Nucl. Fusion 53, 104003A (2013).

‘10’ (Fig. 1 and Fig. 2 (a)). The outer dimensions of a single probe are shown in Fig. 2 (b) and (d), where the coil and the cable connection is also displayed. The coil is soldered with a vacuum compatible solder to a pair of copper clamps to ensure a good electrical connection (Fig. 2 (c) and (d)). The coil itself is a vacuum-compatible inductor from Sumida (series 5120, 8 turns, 7 mm outer diameter, inductance L = 177 nH, quality Q = 120 @ 30 MHz [ref 10]). The inductor is connected via a vacuum-compatible triaxial 50 Ω cable from elspec GmbH (series TR31601, 3.56 mm outer diameter, 1.4 dB attenuation per 10 m @ 30 MHz [ref 11]). The outermost conductor of the cable is grounded to the stainless steel probe body and, hence, to the common ground of Sector 11 (Fig. 2 (d)). The inner most and the 2nd innermost conductors of the cable are crimped to a pair of terminals and then bolted to the two coil copper clamps via a PEEK insulating mounting plate (Fig. 2 (c)). RF signals enters the probe through a 1 mm × 10 mm slit (Fig. 2 (b)). A 1 mm thick ceramic plate is placed between the slit and the coil to prevent direct contact between plasma and the coil (Fig. 2 (c)). The final position coordinates (major radius R, vertical position Z, and toroidal angle ϕ_{tor}) of the probe array were measured with a sub-mm accuracy using a FARO coordinate measuring machine [ref 12].

Amplitude and phase (ϕ) are two of the fundamental properties of an RF wave. The measurement of the amplitude and the phase difference ($\Delta\phi$) between a pair of RF coils/signals is achieved using a two-channel (U1 and U2) logarithmic (log) RF detector. The RF amplitude is converted into a DC signal using an rms-responding power detector stage from Analog Devices (AD8362 [ref 13]), as shown in Figure 3 (a). The phase difference between two RF signals is converted into a DC signal using a phase detector stage from Analog Devices (AD8302 [ref 14]). Note that the phase detector stage is based on an exclusive OR gate technique to detect the phase difference between a pair of RF signals and, as a result, can only unambiguously measure $\Delta\phi$ up to 180^o [ref 14]. To detect $\Delta\phi$ up to 360^o, the input phase of U1 was shifted by 90^o and $\Delta\phi$ was measured simultaneously between U1 and U2 and between U1+90^o and U2, as shown in Fig. 3 (b). Additionally, note that the output of the phase detector stage reaches a stable value only when the amplitude of the two RF input signals is above a threshold value U_{out} = 0.75 V, equivalent to the input power of approximately -30 dBm at the detector (Fig. 3 (c)). The frequency response range of the log detector and the B-dot probe is limited to 10-50 MHz. This bandpass limit is set by a combination of high and low pass filters in the log detector. The Q response of the coil is also measured and found to be in agreement with the specifications provided by the manufacturer [ref 10].

To convert raw amplitude signals measured by the probes to absolute quantities, it is necessary to measure a known RF field. The absolute response of the probes to a known RF B-field was calibrated using a 9”, 50 Ω coaxial transmission line, excited with a 30 MHz signal of a known power and terminated with a 50 Ω load. The probes were placed at the radial location of the transmission line outer conductor and oriented either parallel (//) or perpendicular (⊥) to the excited B-field orientation (azimuthal). The probes were connected to a log detector using the final assembly of in-vacuum triaxial cables, where each is 4 m long. The resulting calibration curves of a typical probe and in-vacuum cable assembly is shown in Fig. 4. The curve for the probe orientation ⊥ to RF B-field remains at 0 V, as expected for a coaxial transmission line.

*For authors list, see U. Stroth et al., Nucl. Fusion 53, 104003A (2013).

This result demonstrates that 1) the coil is well-aligned inside the probe housing and 2) the coil is well-shielded by the stainless steel housing from electrostatic fields. The following relation is used to relate the total time-averaged power ($|P_{av}|$) flowing through the transmission line and the time-averaged Poynting flux (P) at the probe location:

$$P = \frac{|P_{av}|}{2\pi b^2 \ln\frac{b}{a}}$$

where b is the radius of the outer conductor of the transmission line (b = 0.114 m) and a is the radius of the inner conductor (a = 0.050 m). The phase shifts between individual probe and in-vacuum cable assemblies in the HFB probe array were also measured and found to be $<5^o$, low enough to be ignorable. Outside the vacuum vessel the probe array is connected via direct current (DC) breaks and 22 m long low-loss LMR-400-UF cables (~0.6 dB attenuation at 30 MHz) to the log detectors inside an instrumentation rack. Additionally, individual probe signals are split via 3 dB power splitters and attenuated by 10 dB attenuators before entering the input terminals of the log detectors. The total attenuation of the RF probe signals outside the vacuum vessel is ~14 dB. The DC outputs of the log detectors are digitized using a real-time data acquisition system based on a serial input/output (SIO) computer interface [ref 15]. The raw DC signals are sampled by the SIO system at 200 kHz with a 16 Bit resolution over a ± 10 V range.

Experimental Method:

The method used to reconstruct the dominant wavenumber k of the local RF field from the wave phase and position measurements is outlined below. From the definition of the phase $\phi \equiv kx - \omega t$, where x is the distance, ω is the angular frequency of the wave, and t is time, the dominant wavenumber k is obtained from the slope of the $\phi = \phi(x)$ curve, i.e. $k = d\phi/dx$. The frequency dependence does not enter this equation as long as the wave phase is sampled simultaneously at the measurement points. An example of this method is shown in Fig. 5, where k was measured for an RF wave (source frequency f = 30 MHz) propagating in air inside a 9", 50 Ω transmission line. The measured $|k| = 0.621 \pm 0.043$ m^{-1} agrees with the expected value $k = \omega/c = 2\pi \times 30e6$ Hz / 3e8 m/s = 0.628 m^{-1}, where c is the speed of light in air.

Low power near-field RF measurements immediately in front of the Faraday screen of a 3-strap antenna were performed using a Wandel & Goltermann RF field radiation meter ([ref 16] series EMR-20) in order to estimate the dominant wavenumber of the launched ICRF waves for various cases of strap amplitude ratio and strap phasing. The measurements were performed in air and, as a result, the RF power coupling was low, typically <20% of the power provided by the source. In order to minimize the impact of the reflected power on the near-field RF wave distribution, the following procedure was followed. Either the central strap or the side straps were powered, while the remaining strap was terminated with a 50 Ω load. The corresponding time-averaged values of the Poynting flux measurement immediately in front of the Faraday screen of the 3-strap antenna are shown in Fig. 6 (a) and (b). These profiles were then used to calculate the RF B-field profiles, assuming that the dominant field component is toroidal and the vacuum relation holds between the time-averaged Poynting flux P and the RF B-field: $|\text{B-RF field}| = \sqrt{(2\mu_o P/c)}$, where

μ_o is the vacuum permeability. The cases of dipole (0, π, 0) and monopole (0, 0, 0) strap phasing, where the peak RF B-field ratio between the central and the side straps is 2, are shown in Fig. 6 (c). The phase shifts between the two strap contributions are 180^o and 0^o for the dipole and monopole cases, respectively, and are assumed to be constant across the entire antenna surface. The resulting dominant launched toroidal wavenumbers (k_{tor}) are ~9 m^{-1} and ~1 m^{-1} for the dipole and monopole cases, respectively (Fig. 6 (d)). Note that the monopole case has a secondary k_{tor} at ~20 m^{-1} (Fig. 6 (d)).

Experimental Results and Discussion:

The first data with the new HFB probe array diagnostic was obtained during the conditioning phase of the 2015-2016 experimental campaign on ASDEX Upgrade. The discharges were ELMy H-modes (on-axis magnetic field B_T = -2.0 – -2.5 T, total plasma current I_P = 0.8 – 1.0 MA, lower single null configuration). The negative direction of B_T indicates that the magnetic field is in the opposite direction to the plasma current direction. The hydrogen fraction (H/D) was <8%, as measured by a passive neutral particle analyzer operated in the thermal energy regime [ref 17]. The low H/D fraction ensured good ICRF single pass absorption in the hydrogen minority scheme at either 30.0 MHz (for the case of B_T = -2.0 T) or 36.5 MHz (for B_T = -2.5 T).

Changes in strap phasing are expected to have a strong impact on the dominant wavenumber launched by an ICRF antenna. Fig. 7 shows the variation of the local ICRF field properties during a strap phasing scan on the 3-strap antenna, the data is shown for between-ELM periods only. The ICRF power (1.4 MW) and the central- to-side strap amplitude ratio (~2) were kept constant. The strap phasing was scanned by +25/-35^o away from the dipole configuration (Fig. 7 (a)). The resulting phase change of the local ICRF field shows an increase away from the dipole configuration (Fig. 7 (b) and (e)), implying an upshift in the measured local $k_{//}$ (Fig. 7 (f)). The local ICRF field amplitude changes reveal that the amplitude minimum occurs not at the dipole configuration but at +10–15^o away from the antenna dipole configuration (Fig. 7 (c) and (d)). Note that the local ICRF wave amplitude became too low during $0^o < \Delta\phi_{\text{Strap phasing}} < 25^o$ for a reliable phase change measurement with the log detectors, which resulted in a large scatter of the data (Fig. 7 (b) and (e)). The expected k_{tor} values, as estimated from in-air near-field measurements (Fig. 6) are also shown with blue crosses (Fig. 7 (e)). The observed upshift in $k_{//}$ as the strap phasing is changed away from the dipole configuration is consistent with the increase in the amplitude of the local ICRF fields: the launched ICRF wave coupling/accessibility to the core begins to drop exponentially as $k_{//}$ increases resulting in an exponential rise in the wave power deposited in the boundary plasma (Fig. 7 (d)). The trend in the expected k_{tor} value is in the opposite direction to the measured $k_{//}$ trend. However, the in-air near-field measurements do not account for the effect of induced RF fields in the antenna box on the launched $k_{//}$ [ref 18], which likely differ between a poorly matched vacuum case and a well-matched case in the presence of plasma. It is also possible that the local RF fields (which are measured toroidally between two limiter structures) become modified by the conducting boundaries in Sector 11 of ASDEX Upgrade, thereby losing information on the launched ICRF wave properties.

In order to avoid coupling between the 3-strap and 2-strap antennas, when powered simultaneously, the 2-strap antenna operating frequency is set at 1 kHz higher than the nominal

frequency. As a result, we expect to observe 1 kHz beat waves in discharges heated with both ICRF antennas. These waves are, in fact, observed on both the fast wave and the slow wave probes (Fig. 8 (a)). Although the fast wave signal expectedly dominates, the non-zero amplitude of the slow wave beats suggests that the two waves are coupled outside the active antenna [ref 19]. The spectral analysis in the frequency domain reveals the interaction between edge localized modes (ELMs), which peak near 100 Hz, and beats with a mode appearing near 1100 Hz (Fig. 8 (b)). This mode is not present when only one of the antennas is energized.

Overall, the signals on the new HFB probe array show the expected response to the changes imposed by the source – the ICRF antennas. A strap phasing scan away from the dipole configuration reveals a phase response of the local ICRF fields consistent with an upshift in local $k_{//}$. The exponential rise in the amplitude response is also in agreement with the observed $k_{//}$ trend. Operating the two ICRF antennas simultaneously generates 1 kHz beat waves, as expected; however, the beats are observed on both the fast and the slow wave probes pointing that the two waves may be coupled outside the active antennas.

Conclusion:

A new B-dot probe-based diagnostic has been designed, constructed, installed, and successfully operated in ICRF-heated discharges on ASDEX Upgrade. The purpose of the diagnostic is to characterize ICRF wave field properties (their amplitude, polarization, and wavenumber) in the boundary of ICRF-heated discharges. The diagnostic has been installed on the low field side of ASDEX Upgrade in Sector 11 in the toroidal vicinity of two ICRF antennas (Fig. 1). The probe array consists of six B-dot probe pairs, field-aligned to a standard ASDEX Upgrade discharge (Fig. 2 (a)). Each pair has a probe aligned parallel and perpendicular to the local B-field direction to be sensitive to fast and slow ICRF B-fields, respectively. The probe array is connected to a rack of absolutely calibrated log detectors, the purpose of which is to convert RF signals (their amplitude and phase) into DC signals. The DC signals are then digitized and stored for data analysis. The probe response to a known RF B-field has also been absolutely calibrated on a 9", 50 Ω coaxial transmission line.

ICRF strap phasing scans with the 3-strap antenna reveal that the wavenumber of the local ICRF fields becomes upshifted as strap phasing is moved away from the dipole configuration (Fig. 7 (f)). At the same time the amplitude of the local ICRF fields increases exponentially (Fig. 7 (d)), which is consistent with the observed $k_{//}$ upshift. The expected k_{tor} spectrum trend, reconstructed from in-air near-field measurements (Fig. 6), is in the opposite direction (Fig. 7 (f)); however, the reconstructed spectrum does not account for RF currents induced in the passive antenna structures. It is also possible that the local ICRF fields become modified by surrounding conducting structures and, as a result, show a different wave spectrum as the one expected from the simple in-air prediction. Measurements in discharges heated with the 3-strap and 2-strap antennas simultaneously reveal the existence of beat waves (Fig. 8), the frequency of which (1 kHz) is equal to the difference between the operating frequencies of the 2-strap and 3-strap antennas. The beats are observed on both the fast wave and the slow wave probes, suggesting that the two wave fields may be coupled outside the active antennas.

*For authors list, see U. Stroth et al., Nucl. Fusion 53, 104003A (2013).

The HFB probe array is currently being complemented by individual probe pairs in other Sectors, with probes in Sector 1 and 3 already installed. The purpose of these additional pairs is to reconstruct the global toroidal distribution of fast and slow ICRF fields in the boundary of the low field side of ICRF-heated discharges on ASDEX Upgrade. It will then be possible to constrain the development of global three dimensional ICRF wave simulations on ASDEX Upgrade.

Acknowledgments:

This work has been carried out within the framework of the EUROfusion Consortium and has received funding from the Euratom research and training programme 2014-2018 under grant agreement No 633053. The views and opinions expressed herein do not necessarily reflect those of the European Commission. The author and the co-authors would also like to acknowledge the contributions of Bertram Brucker, Johann Kneidl, and Gerhard Siegl in the design, the manufacture, the assembly, and the installation of the HFB probe array on ASDEX Upgrade.

References:

[1] L. Colas, A. Argouarch, S. Brémond, et al., Journal of Nuclear Materials **438** (2013) S330–S333.

[2] D.A. Pappas, B. Lipschultz, B. LaBombard, M.J. May, C.S. Pitcher, Journal of Nuclear Materials **266-269** (1999) 635-641.

[3] Vl. Bobkov, F. Braun, L. Colas, et. al., Journal of Nuclear Materials **415** (2011) S1005–S1008.

[4] A. Ekedahl, L. Colas, M.L. Mayoral, et. al., 15th Topical Conference on Radiofrequency Power in Plasmas, Moran USA, May 19-21 2003.

[5] H. S. Butler and G. S. Kino, Phys. Fluids **6**, 1346 (1963).

[6] J. Reardon, P.T. Bonoli, M. Porkolab, Y. Takase, S.J. Wukitch, 39th Annual Meeting of the American Physical Society, Division of Plasma Physics, Pittsburgh USA, November 17-21, 1997.

[7] M. Ichimura, H. Higaki, S. Kakimoto, Y. Yamaguchi, K. Nemoto, M. Katano, M. Ishikawa, S. Moriyama and T. Suzuki, Nucl. Fusion **48** (2008) 035012.

[8] R. Van Nieuwenhove et al., 16th European Conference on Controlled Fusion and Plasma Physics, Venice Italy, March 13-17 1989.

[9] V. Bobkov, M. Balden, R. Bilato, et al., Nucl. Fusion **53** (2013) 093018.

[10] Sumida catalog, Highly Constant Ceramic RF Coils, pgs. 116-126.

[11] elspec GmbH eCatalog: http://www.elspec.de/hf-kabel-technologie/hf-technik-datenblaetter/hf-triaxialkabel/hf-triaxialkabel-uebersicht.pdf

[12] http://www.faro.com/de-de/home

*For authors list, see U. Stroth et al., Nucl. Fusion 53, 104003A (2013).

[13] Data sheet for 65 dB TruPwr™ Detector, Analog Devices, series AD8362: http://www.analog.com/media/en/technical-documentation/data-sheets/AD8362.pdf

[14] Data sheet for RF/IF Gain and Phase Detector, Analog Devices, series AD8302: http://www.analog.com/media/cn/technical-documentation/data-sheets/AD8302.pdf

[15] K. Behler, H. Blank, A. Buhler, et. al., Fusion Engineering and Design **85** (2010) 313–320.

[16] Wandel & Goltermann, EMR-20 user manual: https://www.darc.de/uploads/media/Bedienungsanleitung_EMR300_02.pdf

[17] R. Bartiromo, G. Bracco, M. Brusati, G. Grosso, S. Mantovani, B. Tilia and V. Zanza, Rev. Sci. Instrum. **58**, 788 (1987).

[18] M.L. Garrett and S.J. Wukitch, 55th Annual Meeting of the American Physical Society, Division of Plasma Physics, Denver USA, November 11-15 2013.

[19] D.A. D'Ippolito, J.R. Myra, R. Ochoukov and D.G. Whyte, Plasma Phys. Control. Fusion **55** (2013) 085001.

*For authors list, see U. Stroth et al., Nucl. Fusion 53, 104003A (2013).

Figures:

Figure 1

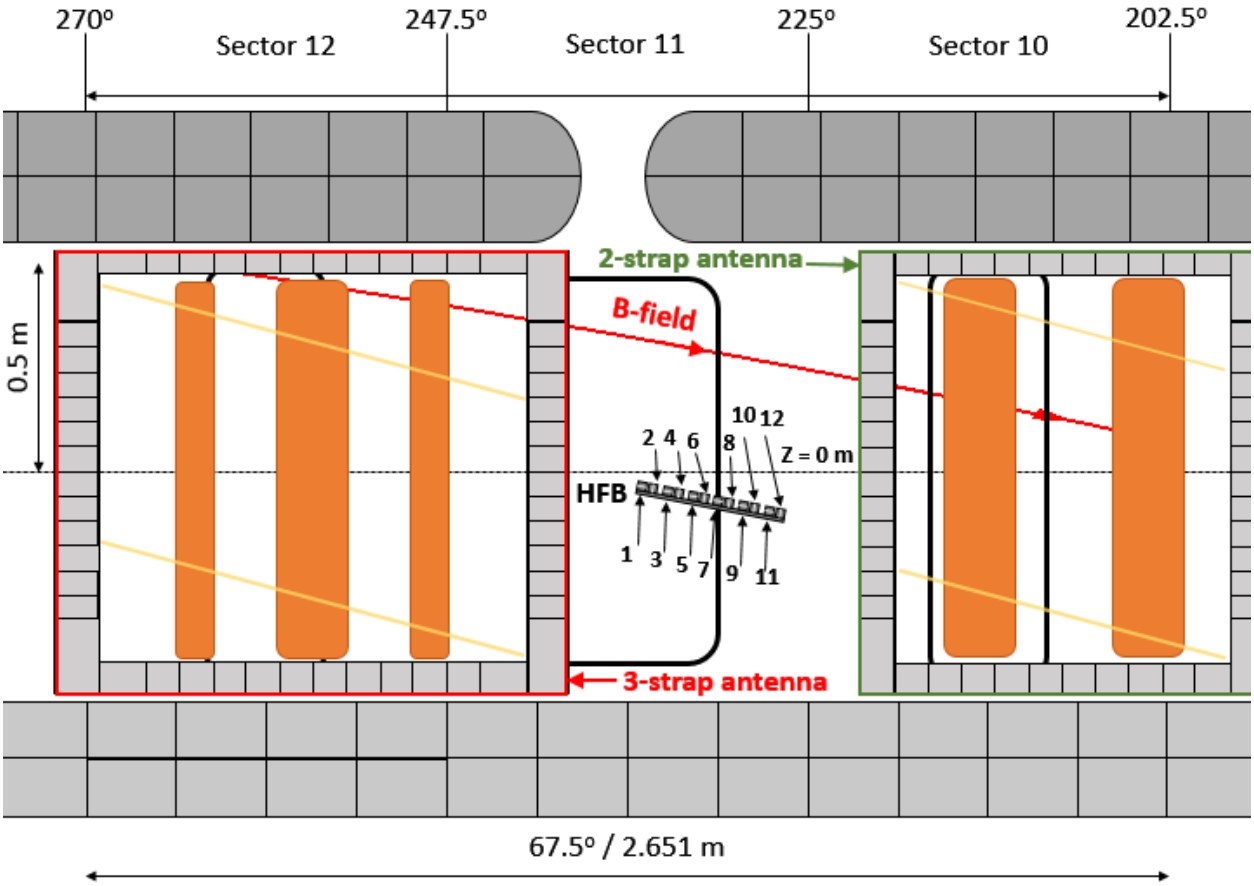

Figure 1: An unfolded view along the major radius R of the outer wall of ASDEX Upgrade. The shown sectors are 10, 11, and 12. The highlighted structures are the 3-strap antenna in Sector 12, the 2-strap antenna in Sector 10, and the high frequency B-dot (HFB) probe array in Sector 11. The red solid line with an arrow shows the contour and the direction of the local magnetic field line (B-field) in a standard ASDEX Upgrade discharge (B_T = –2.5 T, I_P = 1.0 MA). The midplane (Z = 0 m) is shown with a dashed black line. Yellow solid lines across antennas indicate the inclination of the antenna Faraday screen (not shown). The probe array is inclined by ~11° to the midplane. Numbers '1' through '12' refer to individual probes in the HFB probe array, see Fig. 2 for more details.

*For authors list, see U. Stroth et al., Nucl. Fusion 53, 104003A (2013).

Figure 2

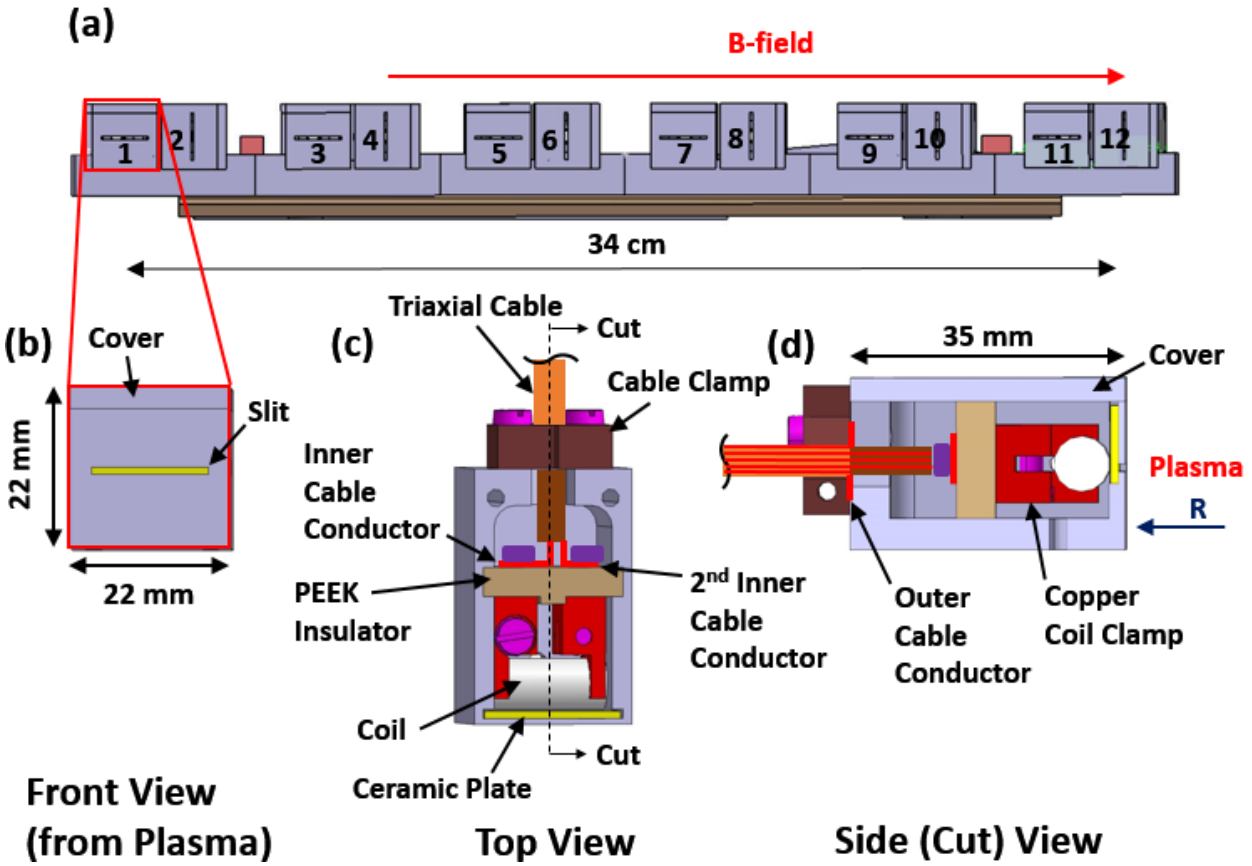

Figure 2: (a) A detailed view along the major radius R of the HFB probe array. The probe array is aligned to the local contour of the magnetic field line (B-field) for a standard ASDEX Upgrade discharge (B_T = –2.5 T, I_P = 1.0 MA). The "fast" wave probes are labeled '1', '3', '5', '7', '9', and '11'; the "slow" wave probes are labeled '2', '4', '6', '8', '10', and '12'. The overall length of the probe array along B-field is shown. (b) A front view (from the plasma along R) of a single probe. (c) A top view of a single probe with the top cover removed and internal components shown. (d) A side (cut) view of a single probe, the direction of R is shown. The overall dimensions of a single probe are also shown.

*For authors list, see U. Stroth et al., Nucl. Fusion 53, 104003A (2013).

Figure 3

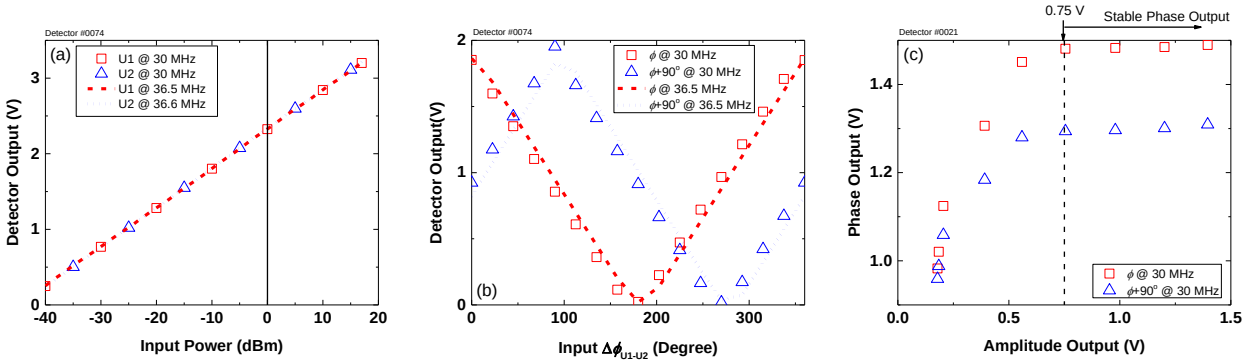

Figure 3: Typical response functions of a two-channel logarithmic RF detector. (a) The output of the amplitude detection stage for channel 1 (U1) and channel 2 (U2) @ 30 MHz and 36.5 MHz vs. the input RF power. (b) The output of the phase detection stage as a function of the input phase difference between U1 and U2 and between U1+90^{o} and U2 @ 30 MHz and 36.5 MHz. (c) The output of the phase detection stage as a function of the output of the amplitude stage. The threshold amplitude value above which the output of the phase detector stage is stable is shown.

*For authors list, see U. Stroth et al., Nucl. Fusion 53, 104003A (2013).

Figure 4:

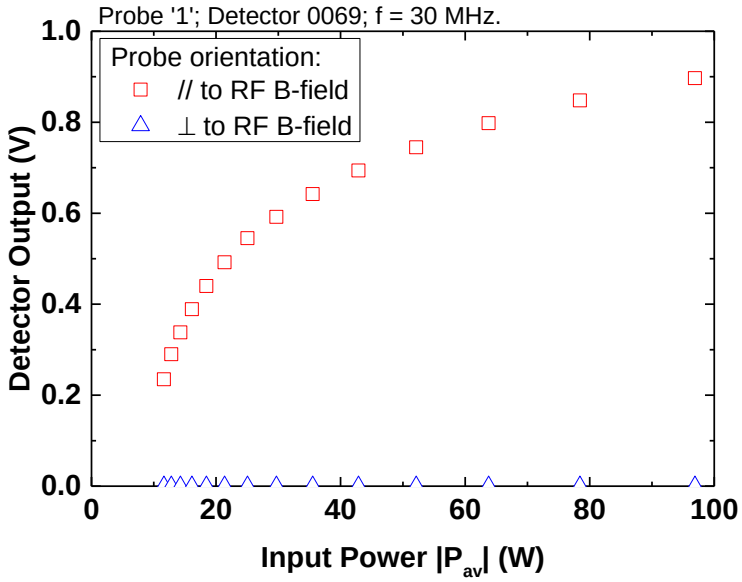

Figure 4: Calibration curves of Probe '1' positioned at the radius of the outer conductor of a 9", 50 Ω coaxial line. The curves are shown for the orientation of the probe parallel (//) to the excited RF B-field (open red squares) and perpendicular (⊥) to the excited RF B-field (open blue triangles). The coaxial line is terminated with a 50 Ω load.

*For authors list, see U. Stroth et al., Nucl. Fusion 53, 104003A (2013).

Figure 5

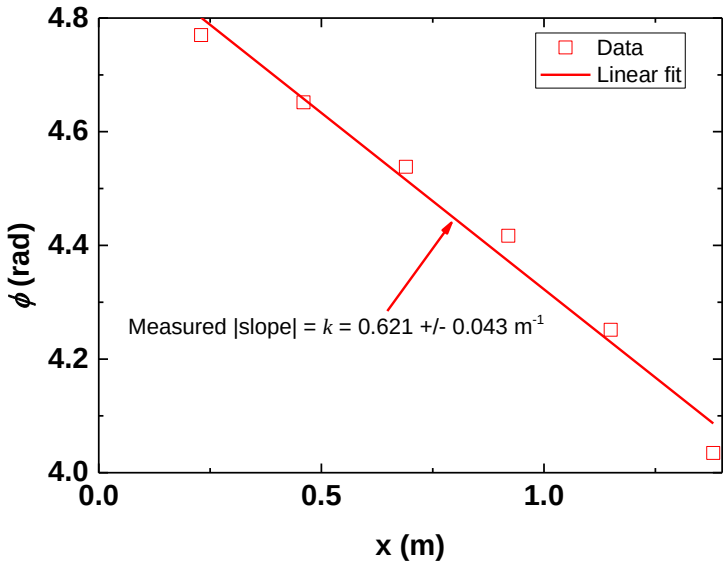

Figure 5: An example of a $|k|$ measurement of an RF wave travelling along a 9", 50 Ω transmission line in air. The open red squares are measurements and the solid red line is a linear fit. The RF frequency is 30 MHz.

*For authors list, see U. Stroth et al., Nucl. Fusion 53, 104003A (2013).

Figure 6

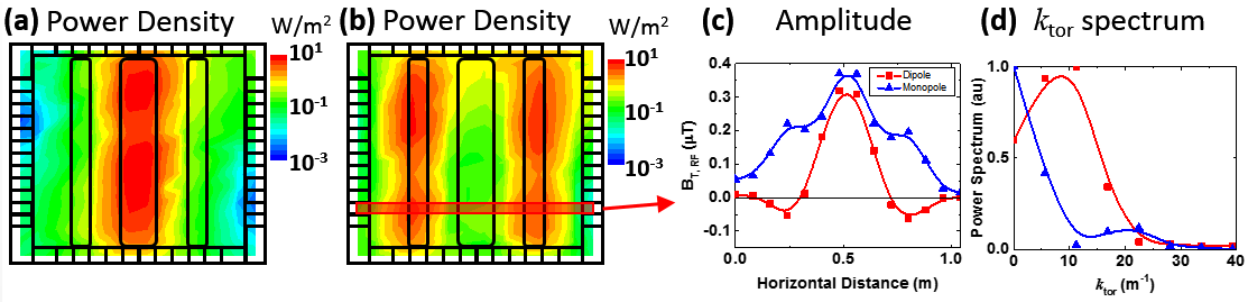

Figure 6: The time-averaged Poynting flux *P* measurements immediately in front of the Faraday screen of a 3-strap antenna for the case of (a) the central strap powered by ~10 W and the side straps terminated by 50 Ω and (b) the side straps powered by ~10 W and the central strap terminated by 50 Ω. (c) The resulting RF B-field amplitude profile along the row highlighted in (b) for dipole (0, π, 0) and monopole (0, 0, 0) strap phasing. The peak RF B-field amplitude ratio between the central and side straps is 2. The dominant RF B-field component is assumed be toroidal and the relation between RF B-field and *P* is assumed vacuum-like. (d) The resulting launched toroidal wavenumber (k_{tor}) spectra for dipole and monopole strap phasing.

*For authors list, see U. Stroth et al., Nucl. Fusion 53, 104003A (2013).

Figure 7:

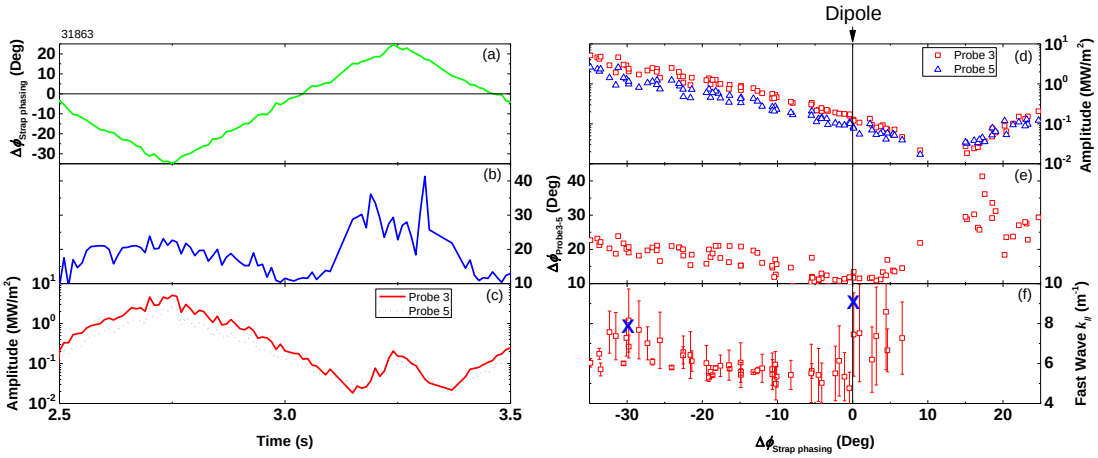

Figure 7: An example of a strap phasing scan on the 3-strap antenna at constant ICRF power and constant strap amplitude ratio. (a) The time history of the 3-strap antenna strap phasing ($\Delta\phi_{\text{Strap phasing}}$). (b) The time history of the phase shift between probes 3 and 5 ($\Delta\phi_{\text{Probe3-5}}$). (c) The time history of the local ICRF field amplitude at probes 3 and 5. (d) The local ICRF field amplitude as a function of the 3-strap antenna strap phasing. (e) The phase shift between probes 3 and 5 as a function of the 3-strap antenna strap phasing. (f) The measured dominant fast wave wavenumber ($k_{//}$) as a function of the 3-strap antenna phasing. The measurement is based on the phase shifts between probes 1 and 3, probes 3 and 5, and probes 5 and 7. The k_{tor} values expected from in-air near-field measurements (Fig. 6) are shown as blue crosses at $\Delta\phi$ = -30° and 0°. The ICRF power was constant at 1.4 MW.

*For authors list, see U. Stroth et al., Nucl. Fusion 53, 104003A (2013).

Figure 8:

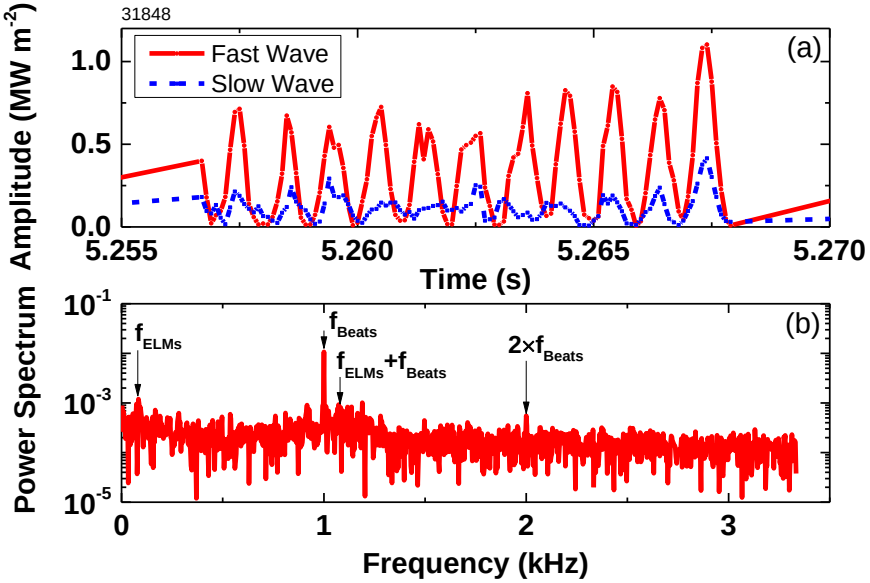

Figure 8: An example of beat waves observed in a discharge heated with the 2-strap and 3-strap antennas simultaneously. The fast and slow wave measurements are from Probe '1' and Probe '2', respectively. The beats are shown in (a) the amplitude and (b) the frequency domain. The total launched ICRF power P_{ICRF} = 3.9 MW. The frequency spectrum reveals edge localized modes (ELMs) at ~100 Hz and the interaction between beats and ELMs at ~1100 Hz. The DC response of the spectrum is suppressed.